Geo-Marine Letters (2021) 41: 17
https://doi.org/10.1007/s00367-021-00684-w

ORIGINAL

Mineralogical, chemical and stable C and O isotope characteristics of surficial carbonate structures from the Mediterranean offshore Israel indicate microbial and thermogenic methane origin

Baruch Spiro[1,2] · Oded Ezra[1] · Jens Najorka[2] · Antonio Delgado[3] · Or Bialik[1] · Zvi Ben-Avraham[1] · Dwight Coleman[4] · Yizhaq Makovsky[1]

Received: 19 May 2019 / Accepted: 13 January 2021 / Published online: 26 February 2021

Abstract

The Eastern Mediterranean continental slope offshore Israel became a focus of exploration for, and production of, natural gas in recent years. The 2010–2011 Nautilus ROV expedition performed detailed video recordings and sampling in two areas offshore Israel: the Palmachim disturbance, southwest of Tel Aviv, and an area offshore Acre, north of Haifa. An analytical programme regarding the carbonate structures was carried out, examining the overall mineralogy, stable C and O isotopes, and Ca, Mg, and Mn concentrations. This provided information on their composition and as a result, an indication of the carbon sources and temperature of formation. The major authigenic minerals identified comprised magnesian calcite, dolomite, aragonite, and kutnohorite. The detrital minerals included quartz, clays, feldspars, and rare augite and enstatite, likely transported from the Nile estuary. The carbon isotope composition of aliquots taken from nineteen samples from these areas have an overall $\delta^{13}C$ range from −62.0 to −0.1‰PDB, indicating a range of microbial/biogenic and thermogenic methane contributions. The range of $\delta^{18}O$ from 2.7 to 7.0‰PDB reflects the range of temperatures of formation. The $\delta^{18}O$ characteristics differ among areas. In general, high values; $\delta^{18}O$ >5‰PDB are recorded from area N2 of the Palmachim disturbance, indicating low temperature of formation. Low values of $\delta^{18}O$ (<5‰PDB) were measured from areas W2 and W3 of the Palmachim disturbance, together with samples from area N2 of the Palmachim disturbance, and samples from areas A1 and A2 offshore Acre indicate high temperature origin. Samples from an inactive chimney from area N2 range from pure dolomite to pure magnesian calcite. This trend is linked to $\delta^{13}C$ increase from −39.9 to −0.1‰(PDB), and $\delta^{18}O$ decrease from 6.2 to 4.7‰(PDB). These values indicate a decrease in the methane-derived carbon contribution and an increase in temperature. Kutnohorite, $Ca(Mn^{2+}, Mg, Fe^{2+})(CO_3)_2$ is a major component in samples from Acre, and less so in the Palmachim disturbance. An exploratory investigation of the relationship between Mn/Ca, $\delta^{18}O$ and $\delta^{13}C$ revealed that samples having Mn/Ca < 0.1(wt./wt.) have $\delta^{13}C$<−50‰PDB indicating a microbial methane source, while samples with Mn/Ca > 0.1 have $\delta^{13}C$ between −35 and −22‰PDB suggesting a thermogenic origin. These results suggest that the mineralogical, isotopic δ^{13}, $\delta^{18}O$, and chemical (Mn/Ca indicative of kutnohorite) characteristics of surficial carbonate structures can indicate and distinguish between deep and shallow methane sources in the Eastern Mediterranean.

Keywords Vent carbonates · Eastern Mediterranean · Israel · $\delta^{18}O$, $\delta^{13}C$ $^{87}Sr/^{86}Sr$ · Aragonite · Magnesian calcite · Dolomite · Kutnohorite · Biogenic · Thermogenic methane

✉ Baruch Spiro
2baruch.spiro@gmail.com

[1] Department of Marine Geosciences, Leon H. Charney School of Marine Sciences, University of Haifa, Haifa, Israel

[2] Department of Earth Sciences, Natural History Museum, London SW7 5BD, UK

[3] Instituto Andaluz de la Ciencias de la Tierra CSIC-UGR, 8100 Armilla, Spain

[4] Coastal Institute, University of Rhode Island, Narragansett, RI 02882, USA

Introduction

In recent years, large gas accumulations were discovered in the Eastern Mediterranean, including offshore Israel (e.g. Shaffer 2011). These findings extend the realm of known gas-prone areas in the Nile delta (e.g. Vandré et al. 2007) to the northeast. Analyses of samples from boreholes on the continental slope indicate that the gas is derived from both microbial and thermogenic sources (Feinstein et al. 2002).

This study follows the survey and sampling of the slope offshore Israel during the 2010–2011 E/V (Exploration

Vessel) Nautilus expedition. The ship has several remotely operated vehicles (ROVs) which can carry out photographic documentation, seafloor exploration, and sampling. Following the expedition, a detailed study of the results of the survey of the area of the Palmachim disturbance was undertaken (Ezra 2016). This study focuses on the documentation and interpretation of surface features in key areas in the Palmachim disturbance (Fig. 1), in view of existing information on structural features and geophysical data for this area.

The present exploratory study documents the mineralogy, stable isotope composition (carbon and oxygen), and some chemical features of surficial carbonate structures, presumably associated with methane seeps, in the Eastern Mediterranean. Our aim is to obtain information on gas sources in areas further to the north east, nearer the shore than identified in previously published works (Fig. 1). We make use of a different source of information by incorporating carbonate structures that occur on the seabed; surficial carbonates have been widely used as indicators of methane sources and their properties (e.g., Aloisi et al. 2000; Greinert et al. 2001; Joseph et al. 2013). The samples investigated originate from two areas on the Israeli Mediterranean slope; the large Palmachim disturbance south west of Tel Aviv, and Acre, west of the town of Acre, north of Haifa (Fig. 1). This study explores the mineralogy, stable isotope composition ($\delta^{13}C$, $\delta^{18}O$), and some chemical indicators (Mn, Ca, and their ratio) of surficial carbonates to elucidate their carbon source. These indicators, in conjunction with chemical, mineralogical, geological, and geophysical information, help to decipher more precisely the geological context of the source of the gas, and its pathways in the studied areas.

This study is based mainly on carbon and oxygen isotope composition in carbonates as indications of the carbon source and the source of the transporting fluid. The general carbon isotope systematics of gaseous hydrocarbons can be complex. However, as the dominant hydrocarbon in the study area is methane, a general assignment based on its typical $\delta^{13}C$ values of methane of the dominant sources, microbial ($\delta^{13}C < -55‰$PDB) and thermogenic ($\delta^{13}C > -45‰$PDB), can be applied (e.g. Schoell 1984; Whiticar 1999; Tissot and Welte 1984). Slightly heavier values are recorded in authigenic carbonates associated with methane (e.g. Greinert et al. 2001; Joseph et al. 2013). The isotope composition $\delta^{13}C$ and δD in residual gas and hydrate samples, as produced in laboratory experiments, revealed that the differences were at analytical precision level (i.e. indistinguishable) (Hashikubo et al. 2007).

On a global scale, large amounts of gas exist in shallow sediments along continental margins and in shallow marine sediments. Methane is the most prominent and occurs in three forms: dissolved gas, gas hydrate, and free gas, with changes occurring in response to changes in physical environmental factors. The carbon content of each of these forms can enter and leave the sediments through microbial decomposition of organic matter, anaerobic oxidation of methane in shallow sediments, and seafloor gas venting (Dickens 2003). These sources can contribute to the reservoir of dissolved bicarbonate, which may then form carbonate structures on the seabed. These contain mineralogical, geochemical, and isotopic information indicative of their sources and environment of deposition.

The examination of surficial carbonate structures may provide useful characterisation of potential gas sources in relatively shallow water sediments along continental margins in general. This approach is of wide interest as in many areas, the mapping and modelling of gas occurrence and distribution is relatively understudied, despite the gas potential of many shallow water gas zones being quantified. The results of this study may thus have great potential in their application during the initial stages of exploration and can be used as indicators for deep thermogenic and shallow bacterial sources in the Eastern Mediterranean. These indications may highlight the possibility of reservoirs of gas derived from shallow bacterial sources, in addition to the known reservoirs of gas of thermogenic origin in the region.

Background

The study areas of the Palmachim disturbance and Acre are located close to the Eastern Mediterranean coast of Israel (Fig. 1a, b). The main source of sediments and its organic matter is the Nile River and its large associated delta (Fig. 1). Along the continental margin of the Eastern Mediterranean, the Palmachim disturbance is the largest of a series of submarine slumps that affect the continental shelf and slope. It is located south of Mt Carmel (Katz et al. 2015) and to the south west of Tel Aviv, at 32° 10′ N 34° 30′ E (Fig. 2). It measures approximately 60 km in length and 16 km in width, bounded by faults trending ca 310° (Garfunkel et al. 1979). These fault-related graben structures appear as westward deepening channels (Fig. 2). Closer to the shore, the slump shows features indicative of extensional deformation. The southern boundary consists of normal faults in the near shore area, and reverse faults in the mound area. A topographic low occurs adjacent to the undeformed continental slope to the north and south, and normal faults are found throughout the slump structure. The middle part exhibits compressional features such as topographic mounds of higher elevation relative to the adjacent undeformed continental slope. The toe area is located ca 900 m below sea level. The morphology of the area at the toe is marked by ca. 2 km spaced elongated ridges, 2.5–6 km in length and trending roughly north-south. Seafloor lineaments impinging on these ridges from the northwest and the southwest represent active faults associated with the southern boundary of the Palmachim disturbance (Fig. 2) (Ezra 2016). The sites west of Acre are located in a different structural setting, adjacent to NW-SE

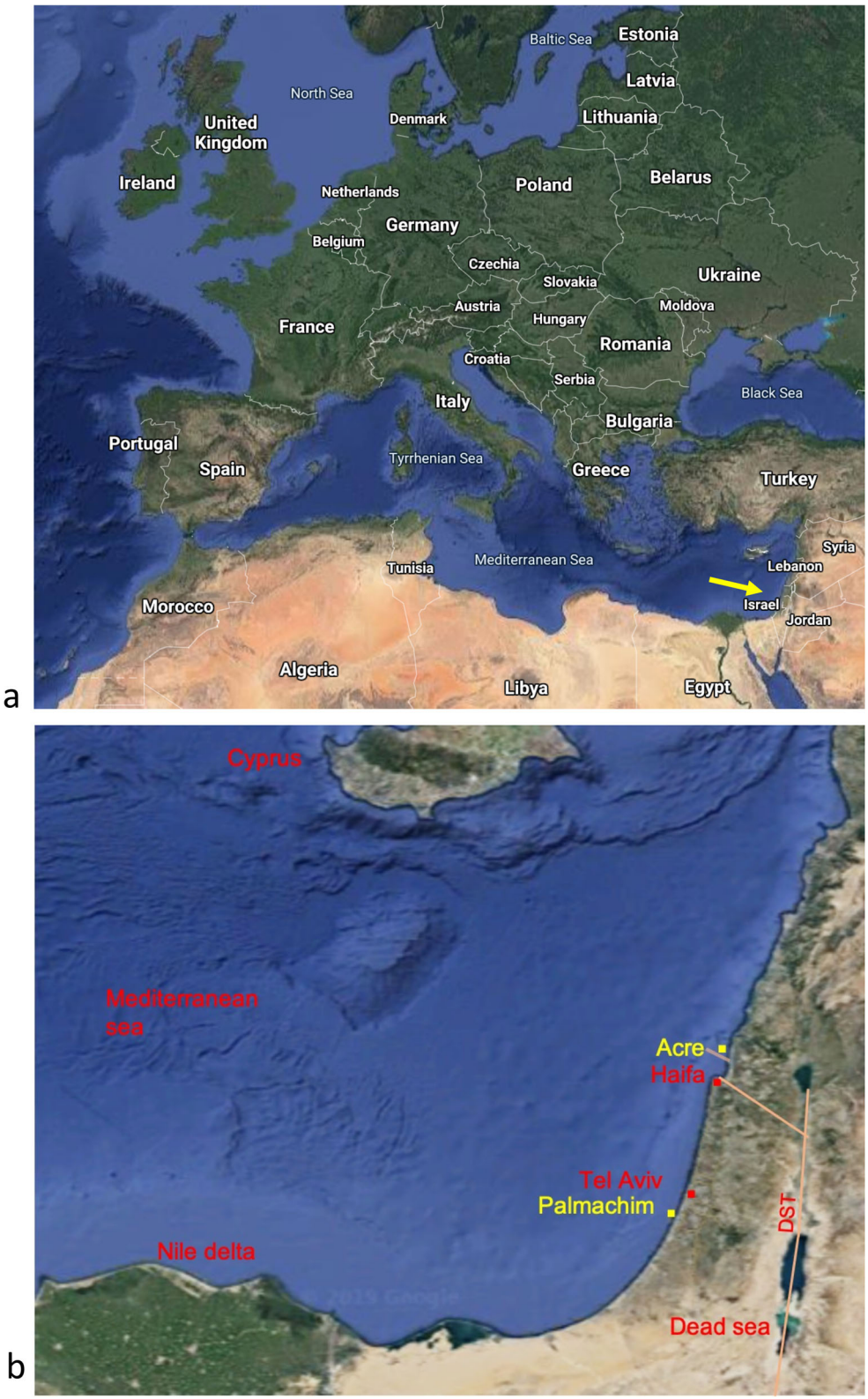

Fig. 1 Maps of the study area. (**a**) Location of Israel. (**b**) Regional map of the Eastern Mediterranean showing key features: the Nile Delta to the south, the shelf and slope areas narrowing towards the north and deeper submarine topographic features. The samples investigated are from the Palmachim disturbance located to the south-west of Tel Aviv, and Acre located to the north of Haifa. The Dead Sea Transform (DST) fault is a dominant tectonic feature in this region. It passes through the Gulf of Eilat (Red Sea), crosses the Dead Sea, and extends northwards through the Jordan Valley. A fault branches to the NW to the Mediterranean Sea at Haifa, and faults belonging to this part of the system occur in the Acre area (Garfunkel 1998)

trending faults that belong of the Dead Sea transform fault (DST) (Garfunkel 1998) (Fig. 1). The DST is part of the Syrian-African Rift System.

The sediments of the Palmachim disturbance are Pliocene-Quaternary in age (Yafo Formation, the upper part of the Saqiye Group). They consist mainly of sediments derived

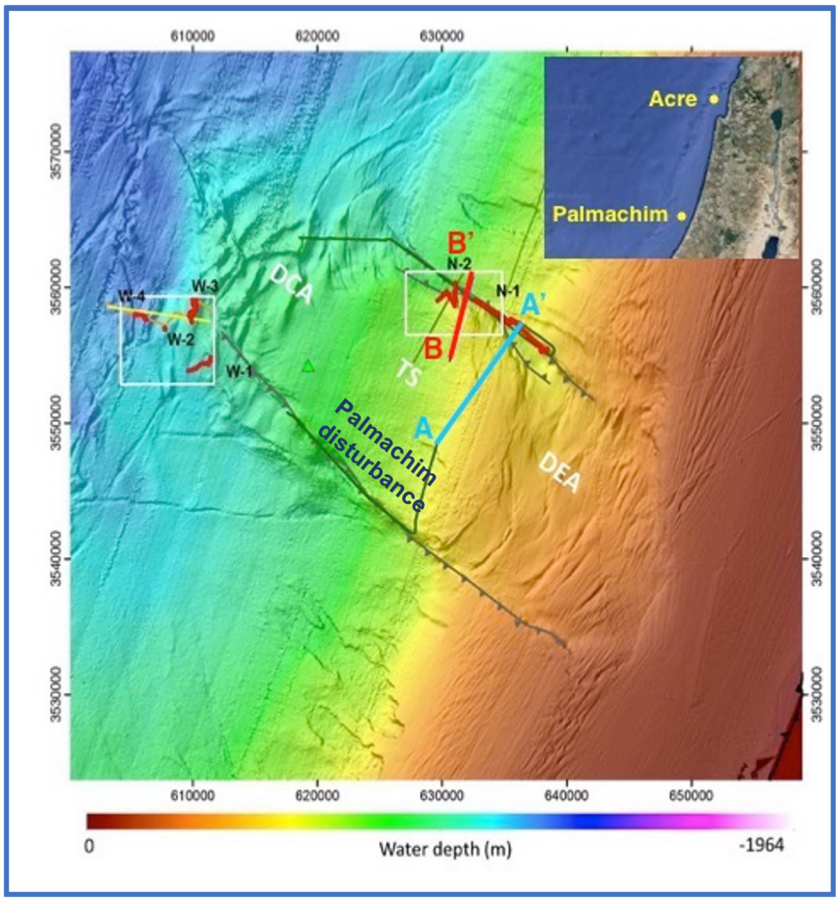

Fig. 2 Inset; location of the Palmachim disturbance and Acre. Main figure; bathymetric map of the area of the Palmachim disturbance: DEA, disturbance extensional area; DCA, disturbance compressional area; TS, translateral slab. Lines A–A' blue and B–B' red indicate the location of the seismic profile shown in Fig. 3 (from Ezra 2016). The white frames indicate the areas investigated by the Nautilus ROV. The northern area is N and the western area is W. The path of the ROV is marked by red lines. Note that in area N, the path of the ROV N2 marked in red is mainly within the TS part of the Palmachim disturbance but it reaches the northern boundary fault and the associated channel. The toe area investigated has a topography reflecting the structural elements of this area. The red lines mark individual path sections of the ROV in the individual areas: N1, N2, W1, W2, W3, and W4. The samples analysed from the Palmachim disturbance were collected in areas N2 W2 and W3. The samples analysed from the Acre area were collected in areas A1 and A2 (Rubin Blum et al. 2014)

from the Nile River, transported by longshore- and offshore-directed currents within the Nile littoral cell (Almagor et al. 2000). In the slump of the Palmachim disturbance, the sediments of the Yafo Formation were detached from the underlying Late Miocene (Messinian) Mavqyim Formation, the lower part of the Saqiye Group. The Mavqiym Formation is rich in evaporites, which were deposited during the desiccation of the Mediterranean. This detachment caused the formation of the offshore slump structures (Garfunkel et al. 1979).

Seismic profiles across the toe of the Palmachim disturbance (Fig. 3) reveal pockmarks that are underlain by high amplitude and reversed phase reflections (Eruteya et al. 2018). These are commonly interpreted as indicators of free gas (Judd and Hovland 1992). These occur at <10 m beneath the sea floor. The Nautilus ROV dives (sites W-2, W-3, and W-4 in Fig. 2) revealed active gas seepages and adjacent carbonate rock formations (Ezra 2016).

The north-western part of the Palmachim disturbance is marked by a steep bathymetric slope descending into the channel that follows its northern boundary fault (Fig. 2). The NE-SW seismic profile across the fault (Fig. 3) indicates that the subsurface sedimentary layers are generally subparallel to the surface of the central part of the Palmachim disturbance. These layers crop out on the northern slope that is formed by the boundary fault (Fig. 3), with terraces having dips of up to 25° towards the south (Ezra 2016). A structural dome underlies the bathymetric mound. This structural position may raise the question as to the source and the time of formation of the carbonate structures detected on that northern slope. They could be related to the beds of the structural dome and formed after its uplift or are related to the boundary fault as a conduit from a deeper source. The samples investigated in this study originate from areas at the toe; W2 and W3 and the northern portion N2, in the Palmachim disturbance, and from areas A1

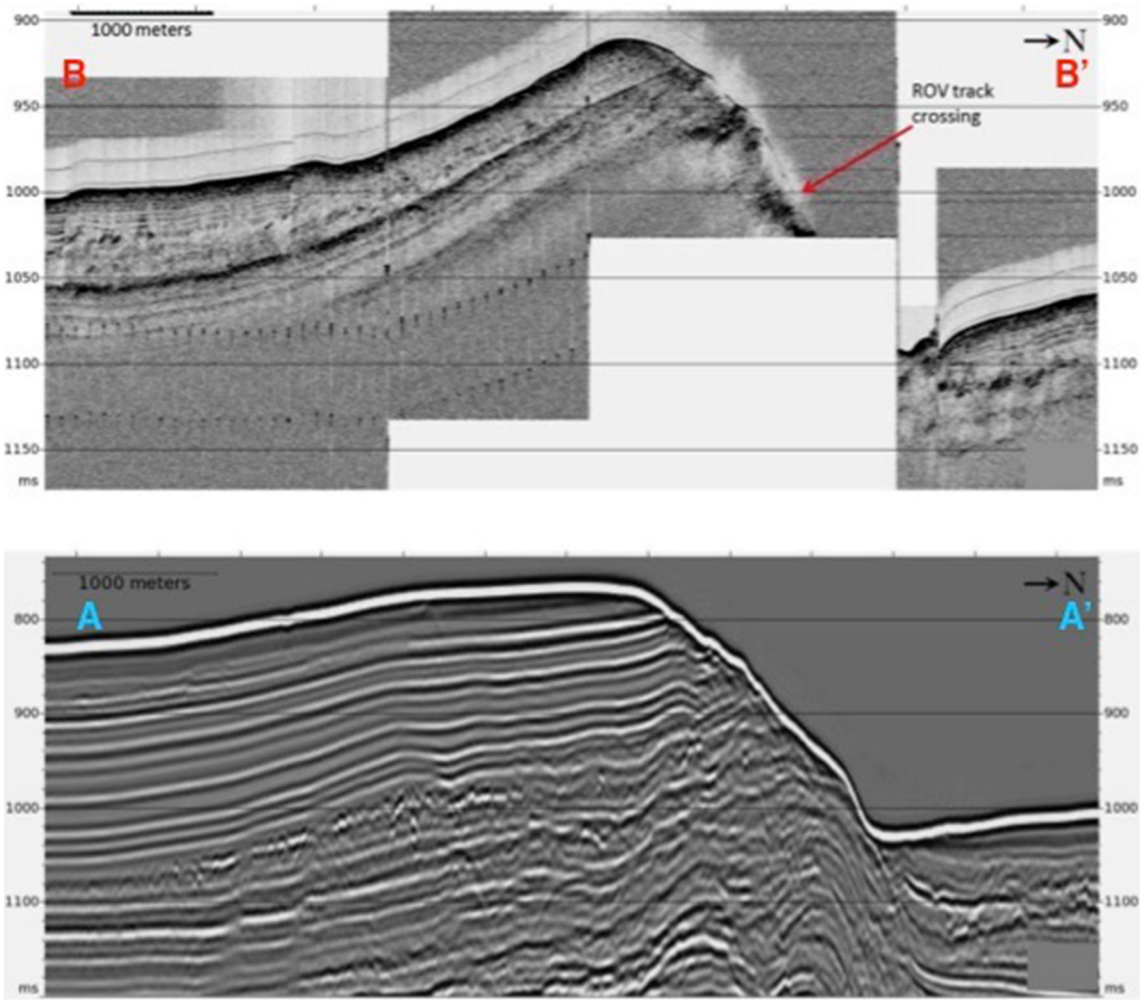

Fig. 3 Seismic profiles across the northern part of the Palmachim Disturbance (locations indicated in Fig. 2). B-B' (Upper) Meteor seismic profile HH20-X-Part-1 (vert. exag. X 10), marked in red, has visible layers down to ~75 m below the seabed. The section crosses the disturbance roughly North-South at the location of the 2010–2011 ROV dive for area N2. Note the bathymetric dome which results from the uplift of the northern edge of the disturbance and the outcrop of the layers of the Yafo Formation (Pliocene-Quaternary), on the northern flank, which is heavily eroded. The carbonate samples collected on this outcrop (path of the ROV shown in area N2 in Fig. 2) indicated low temperature biogenic source, in contrast to samples from the deep channel which indicate thermogenic methane, probably associated with the northern boundary fault. The TGS seismic profile A-A' (Lower) TGS marked in blue in Fig. 2, vertical exaggeration x5, shows the broader topographic and structural features of the area

and A2 of (Rubin-Blum et al. 2014) marked together as the Acre area, offshore the town of Acre (Fig. 1).

Information on gaseous hydrocarbons in the subsurface of the study areas was not found in the literature. However, data on the chemical composition of the gas and the carbon isotope composition of methane, C_2, and C_3 were published for several boreholes from areas offshore southwest of Israel (Feinstein et al. 2002). Results for methane from the Yam-Jaffo 1 borehole, the nearest to the Palmachim disturbance (ca 25 km to the SW), are as follows: for the Pliocene section, the proportion of methane is >99%, $\delta^{13}C$ <−66‰PDB, for the Lower Cretaceous the proportion of methane is >98%, $\delta^{13}C$ −59.6 to −53.8‰, and for the Jurassic the proportion of methane is 35–99%, $\delta^{13}C$ −42.3 to −29.1‰PDB. These results from the Yam Yaffo 1 borehole may be interpreted in view of general assignments of sources of methane as follows: microbial methane $\delta^{13}C < -55$‰PDB, and thermogenic methane $\delta^{13}C > -45$‰ PDB (e.g. Schoell 1984; Tissot and Welte 1984; Whiticar 1999).

Microbiological investigations were carried out in areas offshore Acre and at the toe of the Palmachim disturbance (Rubin-Blum et al. 2014). These included the determination of the concentration and stable isotope composition of methane and sulphate. At the Acre site, the $\delta^{13}C$ values of methane had a minimum value of −80.6‰PDB at 5.5-cm depth indicating microbial origin. The highest sulphate $\delta^{34}S$ value was 53.6‰CDT with $\delta^{18}O$ of 20.4‰ PDB. In comparison, the respective values of sea water samples at that site were 20.3‰CDT and 8.6‰PDB respectively. The high values

are indicative of the effects of bacterial sulphate reduction. At the toe of the Palmachim disturbance, the lowest $\delta^{13}C$ value of methane was −70.4‰PDB at 14-cm depth. The $\delta^{13}C$ values of dissolved inorganic carbon (DIC) ranged from −19.1 at 0.5-cm to −52.2‰PDB at 10.5-cm depth; values indicative of microbial methane (Rubin-Blum et al. 2014).

Materials and methods

The samples collected by the ROV were documented and described on board the ship and kept refrigerated. These were later subsampled for laboratory analysis. Mineralogical analysis by X-ray diffraction (XRD) was carried out at the Natural History Museum London, on powdered samples placed on a zero-background holder (quartz substrate) as suspension in acetone. The XRD measurements were carried out using an Enraf Nonius 590 diffractometer using Cobalt K-alpha1 radiation and a germanium monochromator, a spinning sample stage, and a 120° position sensitive detector (PSD). The angular linearity was calibrated with silver behenate and silicon as external standards. A 2θ linearisation of the PSD was performed with a least-squares cubic spline function. The Hiscore software from Panalytical was used for phase identification along with the PDF database from the International Centre for Diffraction Data.

The stable isotope compositions $\delta^{13}C$ and $\delta^{18}O$ of the carbonate samples was determined at the Instituto Andaluz de Siencia de la Tierra (CSIC-UGR), Granada, Spain, using an XL Thermo Finnigan MAT 251 mass spectrometer. The results are expressed in the δ notation relative to PDB with a precision better than +/−0.1 permil for both $\delta^{13}C$ and $\delta^{18}O$ (Garcia-Alix et al. 2014).

Chemical analyses (Mn, Ca) were carried out at the Natural History Museum London.

Aliquots of about 0.05 g of powdered samples were weighed and then dissolved in concentrated HCL for 1 h at 70 °C. After cooling, the undissolved, solid residue was separated by filtration from the supernatant through 0.2 μm syringe filters. The solutions were then dried and re-dissolved in 1 mL of conc. HNO_3 plus 2 mL of DI H_2O at 70 °C for 1 h. The samples were then made up to 25 ml total volume. The solutions were analysed on an Agilent 7700 ICP-MS

Results

Mineralogical compositions

The carbonate structures have various shapes and sizes (Fig. 4). The sample photographs are marked as a, b, c, etc., and two views (1, 2) are given for each sample except for e. The mineralogical composition is summarised in Table 1 and the diffractograms of mineral assemblages of samples from the various areas are given in Figs. 5, 6, and 7. The stable isotope results are summarised in Fig. 8. The relation between Mn/Ca and the stable isotope composition is given in Fig 9.

The first part of the study focused on carbonate structures of the Palmachim disturbance. One of the largest and most spectacular samples is a chimney, sample 026 (Fig. 4a1), collected in area N2 (Fig. 2). It has a diameter of ca 10 cm with a similar length. A section of the lower part shows the conical chimney structure with a central vertical conduit and horizontal divisions (Figs. 4a1 and a2). A portion of the upper, larger part (Fig. 4a2), was chosen for detailed analysis. Twenty-two aliquots were taken from a polished surface of a lengthwise cut, using a 2-mm diameter drill.

X-ray diffraction (XRD) analysis of these aliquots revealed that they consist of mixtures of only magnesian calcite and dolomite, in a wide range of proportions that span from one nearly pure end member, rich in dolomite, marked as Q188 47, to nearly pure magnesian calcite Q188 48 respectively (Fig. 5). These diffractograms show a slight shift of the main peak of the magnesian calcite to lower 2θ values, indicating an increase in Mg content in the magnesian calcite along with the concomitant decrease in the content of dolomite.

In area N2 of the Palmachim disturbance (Fig. 2), XRD analyses of samples 14B 110 and 013 107 (Fig. 7a) show the presence of kutnohorite, however in lower proportion than magnesian calcite. Also from area N2, sample 025 112 (Pebble) (Fig. 7b) consists mainly of magnesian calcite and dolomite, with minor quartz and traces of montmorillonite. Sample 047A 119 (Branch) consists mainly of magnesian calcite with trace amounts of quartz. Sample 047B 120 (Serpent) consists of magnesian calcite having a wide range of Mg content, and traces of enstatite (Fig. 7b).

In area W2 within the toe of the Palmachim disturbance (Fig. 2), XRD analyses of sample 057a 121 (Fig. 7c) reveal the predominant component to be magnesian calcite, which has a very wide Mg concentration range. It also contains kutnohorite and minor aragonite. Sample 058 112 is dominated by aragonite with calcite and traces of quartz and microcline.

Area W3 adjacent and slightly to the north of area W2 (Fig. 2) is represented by sample 74, which has a layered structure (Fig. 4d). The three layers analysed show the same mineralogical composition of nearly pure magnesian calcite with minor kutnohorite. Sample 077 128 (Karst) consists of aragonite with traces of calcite (Fig. 7d).

Area A1 offshore Acre (Fig. 2) is represented by sample 001B (Wedge) from which five aliquots were taken (Table 1, Fig. 4c1 and c2). The two diffractograms 001B 101 (rusty brown) and 001B 105 (light top) show that kutnohorite $Ca(Mn^{2+}, Mg, Fe^{2+})(CO_3)_2$ is the most abundant mineral, with magnesian calcite the second most abundant, with minor quartz, microcline, and traces of enstatite (Fig. 7a). Rare occurrences of the minerals calcian albite, andesine, and augite of detrital origin were also recorded.

Table 1 Samples and analytical results (arranged according to analysed aliquot number)

Area	Sample no.	Sample name	Analysed aliquot no.	Sample description	$\delta^{18}O$ (‰PDB)	$\delta^{13}C$ (‰PDB)	Mn/Ca (mg/mg)	Q no.	Mineralogical composition
Area N2	026	Large Chimney	LCH1		5.57	−34.80			All aliquots are mixtures of high Mg calcite and dolomite (see Fig. 5)
			LCH2		5.86	−38.94			
			LCH3		5.96	−39.89			
			LCH4		6.04	−34.97			
			LCH5		5.35	−0.10			
			LCH6		5.63	−5.18			
			LCH7		5.17	−22.75			
			LCH8		5.40	−36.00			
			LCH9		5.68	−36.39			
			LCH10		5.73	−36.24			
			LCH11		5.27	−26.91			
			LCH12		5.87	−27.58			
			LCH13		4.68	−25.23			
			LCH14		5.98	−36.82			
			LCH15		6.09	−38.33			
			LCH16		5.51	−31.64			
			LCH17		6.04	−36.40			
			LCH18		5.98	−37.33			
			LCH19		6.04	−36.56			
			LCH20		6.21	−39.26			
			LCH21		5.88	−39.60			
			LCH22		4.85	−22.96			
Area A1	001B	Wedge	101	1 Rusty brown	5.21	−22.82	0.383	19018	Kutnohorite, magnesian calcite (10% Mg), quartz, microcline, kaolinite, montmorillonite
			102	2 Light	5.04	−23.13			
			103	3 Grey lower	5.67	−23.57			
			104	4 Grey upper	4.01	−22.46			
			105	5 Light top	4.47	−22.34	0.198	23037	Kutnohorite, magnesian calcite (10% Mg), quartz, microcline, montmorillonite, enstatite
Area A2	12	Massive	106		4.10	−35.13		19092	
Area N2	013-C	Sandy	107	1 Sandy lower	3.64	−23.56		19019	Magnesian calcite (10% Mg), kutnohorite, quartz, microcline, montmorillonite, enstatite
			108	2 Sandy middle	4.69	−31.27		19093	
			109	3 Sandy upper	4.05	−33.07		19094	
Area A2	014B	Small chimney	110	1 Small chimney inner	4.05	−33.72	0.144	19082	Magnesian calcite (8% Mg), kutnohorite, quartz, microcline, montmorillonite
			111	2 Small chimney outer	6.2	−23.19	0.153	23038	Magnesian calcite (30% Mg), kutnohorite, quartz, microcline, montmorillonite
Area N2	025	Pebble	112	1 Pebble inner	6.32	−15.1		19090	Magnesian calcite (10% Mg), dolomite, quartz, montmorillonite
			113	2 Pebble outer	5.96	−22.04		19091	
Area N2	027A		114		5.35	−31.46			
Area N2	036	Small tree	115	Small tree	5.46	−3.37			
Area N2	041	Moon structure	116	1 moon filling	6.41	−12.78		19085	

Table 1 (continued)

Area	Sample no.	Sample name	Analysed aliquot no.	Sample description	$\delta^{18}O$ (‰PDB)	$\delta^{13}C$ (‰PDB)	Mn/Ca (mg/mg)	Q no.	Mineralogical composition
			117	2 moon inner white	6.76	−62.31	0.044		
			118	3 moon outer grey	6.57	−53.68	0.041	19086	
Area N2	047A	Branch	119		7.00	−28.88		19088	Nearly pure magnesian calcite (10–12% Mg), quartz
Area N2	047B	Serpent	120		6.99	−51.98	0.083	23040	Magnesian calcite (10–18% Mg), quartz
Area N2	049D	Dead bamboo coral	120B		5.73	−36.95			
					5.58	−39.11			
					5.79	−32.65			
					5.09	−36.2			
					5.92	−28.31			
Area W2	057	Hard bed	121		5.82	−48.54		19089	Magnesian calcite (10–20% Mg) aragonite, quartz, kaolinite
Area W2	058	Boring	122		3.44	−25.45		19095	Aragonite, magnesian calcite (13% Mg), quartz
Area W3	061	Bivalve substrate	123		3.88	−22.61		19096	
Area W3	065	Topog	124	Topog lower	3.86	−39.18		19099	
Area W3	067	Topog	125	Topog upper	3.85	−41.79		19100	
Area W3	077	Karst	128		2.57	−33.75		19097	Aragonite, magnesian calcite
Area W3	074	Layered		74(1) lowermost					
			129	74(2) Lowermost cemented 74(3) interlayer not cemented	4.25	−27.49		23043	Magnesian calcite (14% Mg), kutnohorite
			130	74(4) 2nd cemented	4.24	−30.53		18839	Magnesian calcite (14% Mg), kutnohorite
			131	74(5) third cemented	4.8	−20.28		23046	Magnesian calcite (14% Mg), kutnohorite
			132	74(6) uppermost cemented	3.94	−20.99		18841	

Stable carbon and oxygen isotope composition

The 22 aliquots of the chimney sample 026 show an overall trend of decrease in dolomite and increase in magnesian calcite (Fig. 5). The trend of increasing dolomite content is associated with a decrease in $\delta^{13}C$ from −0.1 to −39.9‰PDB and increase in $\delta^{18}O$ values from 4.7 to 6.2‰PDB (Table 1) is represented by six aliquots in Fig. 6. The $\delta^{13}C$ and $\delta^{18}O$ results for the 22 aliquots of sample 026 chimney show an overall trend of decrease in $\delta^{13}C$ values with increase in $\delta^{18}O$, along with the increase in magnesian calcite content (Fig. 7a). Two aliquots stand out. These are dominated by magnesian calcite, having high $\delta^{13}C$ values of −0.1 and 5.2‰PDB respectively. These are in the middle of the $\delta^{18}O$ range 4.7 and 6.2‰PDB (Table 1) (Fig. 4b). These trends in a single chimney indicate changes in the controls of the carbonate system in a single orifice over time, hence a change in source and/or feeding pathway.

The mineralogical and isotopic features and their relations described for the chimney sample 026 of area N2 can be regarded as a reflection of changes at this specific locality in area N2 on the north-facing slope of the channel that follows the large fault bordering the Palmachim disturbance (Fig. 2). The gradation of and the relationship between the two isotopic signatures suggest a continuous change in the contribution of the respective sources and a link between the two parameters. The low values of endmember $\delta^{13}C$ and the concomitant high and increasing values of $\delta^{18}O$ point to methane oxidation

related to bacterial sulphate reduction (e.g. Jørgensen 1977; Aharon and Fu 2000). The relationship between the trends of these values within a single carbonate chimney may indicate a continuous evolution of the system from nearly pure dolomite, with carbon derived from bacterial methane and oxygen influenced by bacterial sulphate reduction, to increasingly seawater-derived carbon in the formation of magnesian calcite. Similar $\delta^{13}C$ $\delta^{18}O$ trends and ranges were reported from dolomitic chimneys in the Gulf of Cadiz (Magalhaes et al. 2012). It is noteworthy that with decreasing proportion of dolomite, the peak of high Mg calcite shifts to the left (decreasing 2θ values) (Fig. 5), indicating an increase in the Mg/Ca ratio.

The patterns of $\delta^{13}C$ and $\delta^{18}O$ of other samples are different from those of sample 026. Patterns of relatively wide ranges in $\delta^{18}O$ values and narrow ranges in $\delta^{13}C$ values, and vice versa, occur in several samples (Fig. 8b). Sample 001B (Wedge), from area A1 (Fig. 2) shows differences in isotopic composition between five aliquots; the overall range of $\delta^{13}C$ is −23.6 to −22.3, while the range of $\delta^{18}O$ values is relatively larger: 4.0 to 5.7‰PDB (Fig. 8b). The four aliquots taken from different layers of sample 074 (layered) (Fig. 4), from area W3 (Fig. 2), have a relatively constant mineralogical composition (Fig. 7d), yet they show a large range of $\delta^{13}C$ −30.6 to −20.3‰PDB with a range of $\delta^{18}O$ values between 3.9 and 4.6‰PDB (Fig. 8b). The five aliquots of sample 049D, the Bamboo coral, from area N2 (Fig. 2) have a $\delta^{13}C$ range of −39.1 to -−28.3‰PDB, and relatively narrower range of $\delta^{18}O$ values from 5.1 to 5.9‰PDB (Fig. 8b).

The overall distribution of $\delta^{13}C$ and $\delta^{18}O$ values given in Fig. 8b shows a range of $\delta^{13}C$ from −62.3 (041 Moon structure) to −0.1‰PDB (026 Large Chimney), and a $\delta^{18}O$ range between 2.7 (077 Karst) and 7.0‰PDB (047a Branch). There does not seem to be an association between sample site and $\delta^{13}C$ values (Table 1). However, there seems to be a division in $\delta^{18}O$ values according to geographic areas. Samples from areas A1, A2, and W3, and most of the samples from area W2 (Fig. 2), have $\delta^{18}O$ values lower than 5‰PDB, while samples from area N2 have $\delta^{18}O$ values higher than 5‰PDB. The range of values of sample 001B from area A1 ($\delta^{18}O$ 4.5–5.2‰PDB) crosses this division in $\delta^{18}O$ values, along with 2 out of the 22 aliquots of sample 026.

The overall $\delta^{18}O$ range in the samples of the present study of the Palmachim disturbance and offshore Acre (3.9–7.0‰ PDB) is similar to the overall range of $\delta^{18}O$ values reported for groups B, C, D, and E from the Hydrate Ridge (2.4–7.8‰ PDB) by Greinert et al. (2001). In contrast, the $\delta^{13}C$ range for the present study (−62.3 to −0.1‰PDB mainly) is wider than the range of $\delta^{13}C$ values of groups B, C, D, and E of Greinert et al. (2001) (−58 to −24‰PDB). The ranges of group A of Greinert et al. (2001), the deep methanogenic zone ($\delta^{13}C$ −5 to −25‰, with $\delta^{18}O$ 4–8‰PDB), and those of the "enigmatic" group F ($\delta^{13}C$ −42 to −58 and $\delta^{18}O$ 11–15‰PDB) are not represented in the present study.

The ranges of $\delta^{13}C$ (−58 to −24‰PDB) and $\delta^{18}O$ (2.4–7.8‰PDB) of the Hydrate Ridge and the ranges in groups B, C, D, and E (Greinert et al. 2001) (the range of $\delta^{13}C$ and $\delta^{18}O$ values group A Deep sources were not recorded in the present study) provide a general reference. However, they should not be regarded as rigid boundaries, particularly in view of the geographic, oceanographic, and climatic differences between the Hydrate Ridge and the Eastern Mediterranean.

Among the four groups of Greinert et al. (2001) (Fig. 8c), group B consists mainly of dolomite and is interpreted as forming in the deepest part of the sulphate reduction zone, transition between sulphate reduction and methanogenesis, i.e. deep methane source. Group C is dominated by proto dolomite and dolomite, formed in the sulphate reduction zone, at intermediate depth. Group D contains dolomite; its carbon is derived from methane and degraded organic matter and is deposited at shallow depths. Group E is dominated by aragonite and is formed by methane oxidation via sulphate reduction, near the surface. Both groups D and E are marked by the absence of dolomite.

A major division in the $\delta^{18}O$ values occurs at 6‰PDB (Fig. 8c). This separates groups B and C from groups D and E. The schematic cross-section of a basin with a major fault—a conduit for deep methane (shown in Fig. 6 of Greinert et al. 2001)—classifies groups B and C characterised by $\delta^{18}O <$ 6‰PDB and the presence of dolomite, to deeper parts of the sediment column in the basin. By contrast, groups D and E, characterised by $\delta^{18}O >$ 6‰PDB with no dolomite, are related to the shallower ones. The study of the Hydrate Ridge (Greinert et al. 2001) shows mineralogical features of carbonates and their $\delta^{18}O$ values as criteria for the distinction between carbonates of deep layers, from those of shallow layers in the methane generating basin.

The results of the present study show a boundary at $\delta^{18}O$ at 5‰PDB (Fig. 8b). This $\delta^{18}O$ boundary may be analogous to the boundary at 6‰PDB in the Hydrate Ridge. This boundary distinguishes between samples with $\delta^{18}O <$ 5‰PDB—indicating warmer fluids, mainly from areas A2 Acre, and W3 and some from W2 the toe of the Palmachim disturbance (where shallow gas was identified by seismic methods), from several samples from area N2 south of the major northern boundary fault of the Palmachim disturbance, with $\delta^{18}O >$ 5‰PDB—indicating shallower colder fluids. The difference in the values of the $\delta^{18}O$ of boundaries, between Hydrate Ridge −6‰PDB and Palmachim disturbance −5‰PDB, may be due to the differences in temperature and depth at the sites. The Hydrate Ridge in the NW Pacific is being colder in contrast to the warmer sites of the present investigation in the Eastern Mediterranean, where the shallow carbonate structures were formed.

In the present study, this boundary at $\delta^{18}O$ of 5‰PDB distinguishes between carbonates formed in sites located in the vicinity of major faults, from carbonates formed in the shallower northern slope of the Palmachim disturbance (area N2), which is located to the south of the northern boundary fault. This area is part of an erosion surface that truncates the up-dip sediment layers of the Palmachim disturbance (Fig. 3). It can thus be suggested that this boundary of $\delta^{18}O$ at 5‰PDB indicates a distinction between sources of fluid: possibly shallow—the sediment layers having outcrops on the southern part of area N2 at Palmachim (see cross-section Fig. 3), in contrast to deep sources for the northern part of area N2 along its northern boundary fault, the other sampling areas of the Palmachim disturbance, and also Acre.

Manganese distribution—kutnohorite

One of the interesting features revealed in this study is the occurrence of the mineral kutnohorite (also kutnahorite), Ca (Mn, Mg, Fe $^{2+}$) $(CO_3)_2$. This mineral is an isotype of dolomite and was detected by XRD analysis of bulk powdered aliquots of several samples. Kutnohorite and other Mn-bearing carbonate minerals are usually associated with epithermal or hydrothermal ore deposits, such the silver deposit at Kutnahora in Bohemia hence the name, and it occurs also in regionally metamorphosed terranes. However, it was also reported from freshwater, marine, and oceanic sediments (Mucci 1991). In the Sea of Okhotzk, it occurs in association with methane plumes derived from gas hydrates (Astrakhov et al. 2008). The present results indicate that the occurrence of kutnohorite in areas of extensive faults may indicate contribution from a deep methane source.

The relationship of Mn/Ca to the $\delta^{18}O$ and $\delta^{13}C$ values in samples with and without kutnohorite shows several interesting results. Four kutnohorite-bearing samples were chosen: 001B-101, 001B-105 from area A1, and 14B-110, 14B-111T from area A2, and compared with three samples in which Kutnahorite was not detected, 41–117, 41–118, and 47B from area N2 (Table 1). The results of the chemical analyses show that the samples in which kutnohorite was detected by XRD had Mn/Ca values of 0.14 to 0.38 wt./wt., whereas samples in which kutnohorite was not detected had much lower Mn/Ca values: between 0.04 and 0.08 wt./wt. The plot of $\delta^{18}O$ and $\delta^{13}C$ of these seven samples (Fig. 9) shows that there is a marked difference between the two groups. The samples in which kutnohorite was detected have $\delta^{13}C$ values higher, and $\delta^{18}O$ values lower, than the samples in which kutnohorite was not detected (Fig. 9a). This distinction is evident in Fig. 9b and c where the samples with low Mn/Ca values (those in which kutnohorite was not detected) have lower $\delta^{13}C$ values < −50‰ PDB and higher $\delta^{18}O$ values >6.7‰, in comparison with samples with higher Mn/Ca ratios in which kutnohorite was detected, which have $\delta^{13}C$ values > −33.7‰ PDB and $\delta^{18}O$ values <6.2‰ PDB (Fig. 9b and c).

A similar general trend was observed for the relation between $\delta^{13}C$ and Mn/Ca values from the Cascadia margin, in the Pacific Ocean, in the offshore area of Washington, USA, and SW Canada (Joseph et al. 2013). It is noteworthy that for the Cascadia Margins, the overall range of $\delta^{13}C$ is −55 to 8‰ PDB and for $\delta^{18}O$ the range is −10 to 5‰PDB.

The chemical indicator Mn/Ca ratio in the samples analysed corroborates the mineralogical indication (by XRD) of the presence or otherwise of kutnohorite. The increase in the Mn/Ca ratio is associated with an increase in the value of $\delta^{13}C$ in the bulk carbonate assemblage which contains kutnohorite. In the two groups of samples chosen for these analyses, the ranges of $\delta^{13}C$ for two sampling areas are different: −62.3 to −52.0‰PDB for samples from area N2—kutnohorite not detected, in contrast to the ranges of $\delta^{13}C$ −33.7 to −22.3‰PDB for the samples from areas A1 and A2, in which kutnohorite is present. The chemical-mineralogical composition and $\delta^{13}C$ values lead to the conclusion that there is a difference between the two groups. The $\delta^{13}C$ values of the carbonates including kutnohorite, in areas A1 and A2 ($\delta^{13}C$ −33.7 to −22.3‰PDB) and many of the samples from areas W2 and W3 (samples 58, 61, 74, 77) ($\delta^{13}C$ −33.7 to −20.3‰PDB) are indicative of thermogenic methane, while those determined from carbonates in samples 57, 65, and 67 (areas W2 and W3) (kutnohoritre not detected) ($\delta^{13}C$ −48.5 to −39.2‰PDB) are indicative of methane of microbial origin. All samples from area N in which kutnohorite was not detected have $\delta^{13}C$ −62.3 to −52.0‰ PDB) indicating a microbial methane origin.

Discussion

This study examined the mineralogical, stable isotopic, and chemical-Mn/Ca ratios as indicators to distinguish between carbonate structures formed from solutions originating from great depth, from those of shallow origin. On this basis, we make comparison with the study of carbonates associated with methane hydrates of the Hydrate Ridge (Greinert et al. 2001) located in a different—colder—climatic zone, in order to juxtapose and compare our findings.

The mineralogical study identified authigenic carbonate minerals as major constituents of the submarine surficial structures. Magnesian calcite shows a wide compositional range (8–30% Mg) and together with dolomite, low Mg calcite and aragonite comprise the minerals common in marine environments. Kutnohorite which occurs widely in hydrothermal mineral deposits was observed in marine carbonate structures associated with methane plumes (Astrakhov et al. 2008).

Non-carbonate minerals (excluding sulphides) include silicates: the clay minerals—montmorillonite, rare kaolinite,

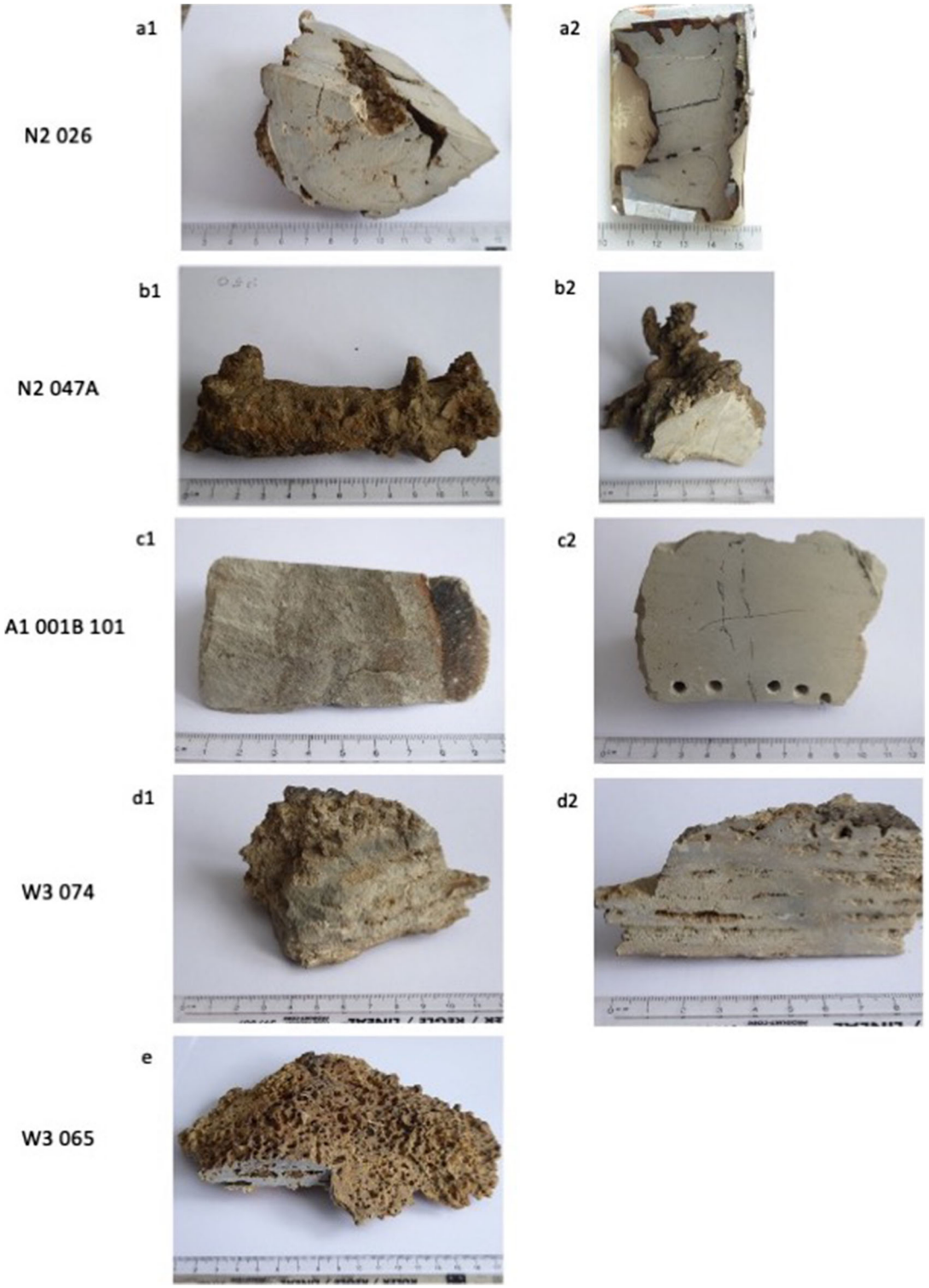

Fig. 4 Photographs of representative carbonate structures from the Palmachim disturbance. The respective data are given in Table 1. **a** Area N2, parts of sample 026 Chimney. (**a1**) The lower part of the chimney having a conical shape, a central conduit, and transverse partitions. (**a2**) Slice of the upper part from which 22 aliquots were analysed. **b** Area N2 sample 47A branch. (**b1**) The sample has an irregular elongated shape. (**b2**) Side view of a cut surface showing a dense massive texture. **c** Area A1 sample 001B 101 wedge. (**c1**) Side view reveals layers, accentuated by weathering. (**c2**) Cut surface perpendicular to layering. Note the lack of layering and holes that mark the sub sample sites. **d** Area W3, sample 74 layered. (**d1**) The eroded surface shows layers of different textures and levels of grey. (**d2**) Cut surface showing the general continuity of the individual layers but gaps occurring between layers. **e** Area W3 sample 065 topography, showing a layered structure with gaps and an irregular, heavily eroded surface

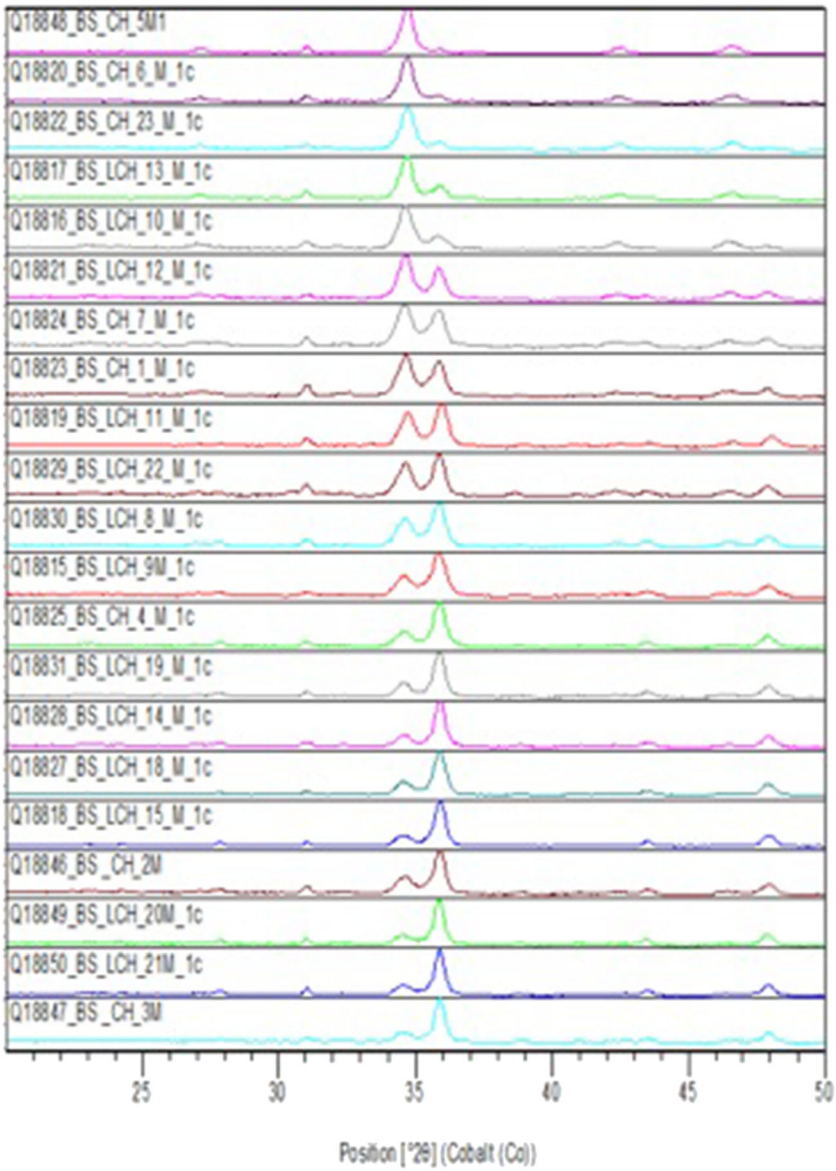

Fig. 5 X-ray diffractograms of 22 aliquots of the chimney sample 026 (area N2) arranged from bottom to top in the order of decreasing intensity of the major peak of dolomite and the increase of the major peak of magnesian calcite. The $\delta^{13}C$ values increase with the increase in magnesian calcite

quartz, feldspars (microcline, calcian albite, andesine), with rare occurrences of augite and enstatite. Most of these minerals, which do not occur in the catchments of the drainage system in this section of the shore of the Mediterranean, are likely to be derived from the Precambrian igneous rocks exposed in the upper reaches of the Nile River (Almagor et al. 2000). Furthermore, organic matter transported from the Nile Delta is the major component of the content of organic matter in shallow sediments along the Eastern Mediterranean coast particularly offshore the Sinai Peninsula and Israel.

As the distribution of $\delta^{13}C$ and $\delta^{18}O$ values of the carbonate minerals provide indicators to the source of carbon and the controls on the isotope composition, a large chimney from area N2 was investigated first. The chimney sample has a range increasing from $\delta^{13}C$ −39.6‰ to 0.1‰PDB associated with $\delta^{18}O$ values decreasing from 6.2 to 4.7‰PDB, while the mineralogical composition, along these trends, vary from nearly pure dolomite to nearly pure magnesian calcite respectively.

The overall range of $\delta^{13}C$ values in the samples of the present investigation is between −62.3 and −0.1‰PDB (mostly < −22.0) and the $\delta^{18}O$ values between 3.4 and 7.0‰PDB. Altogether, these ranges indicate a great variability in the source of carbon and the temperature of the fluid emanating at the sites of deposition, and even changes during the formation of the individual carbonate structures.

These results (Table 1) indicate that in the Acre area (A1 and A2) and areas in the Palmachim disturbance (W2 and W3), the carbonate structures recorded thermogenic methane. Area N of the Palmachim disturbance was influenced by thermogenic methane in the northern portions, close to the boundary fault. The carbonate samples from the southern part of area

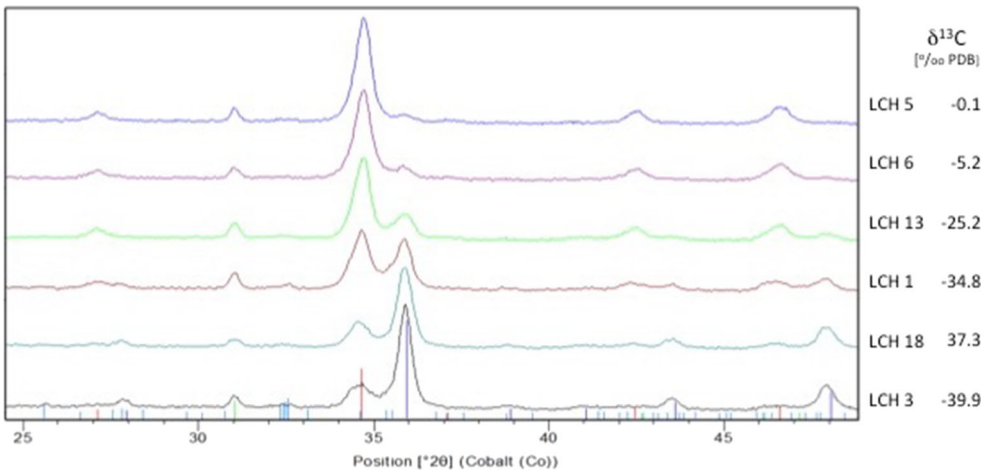

Fig. 6 Trends in the proportions of high Mg calcite and dolomite and $\delta^{13}C$ values in six aliquots of sample 026—chimney. The X-ray diffractograms of six aliquots are arranged from bottom to top of the figure in the order of a decrease in the proportion of dolomite and increase in magnesian calcite. Note that with increasing proportion of dolomite, the $\delta^{13}C$ value of the samples decrease from −0.1‰ to −39.9‰ to PDB

N2 indicate microbial methane probably derived from the shallow sediments exposed on the northern slope of boundary fault.

Furthermore, much of the organic matter was probably derived from the Nile and its large delta. These were transported to the shores of the Eastern Mediterranean by the longshore current (Almagor et al. 2000). Therefore, the study of the isotopic characteristics and the geographical extent of the Nile-derived sediments in the Eastern Mediterranean, and the isotopic characteristics of the related seabed carbonate structures might be important tools for the regional evaluation of potential shallow sources of methane in the Eastern Mediterranean (Praeg et al. 2011).

An intriguing question concerning the seabed carbonate structures is the temporal changes in sources and in the conditions prevailing at their site of deposition over time. The large chimney (sample 26) (Fig. 4a) from area N of the Palmachim disturbance showed variations from nearly pure

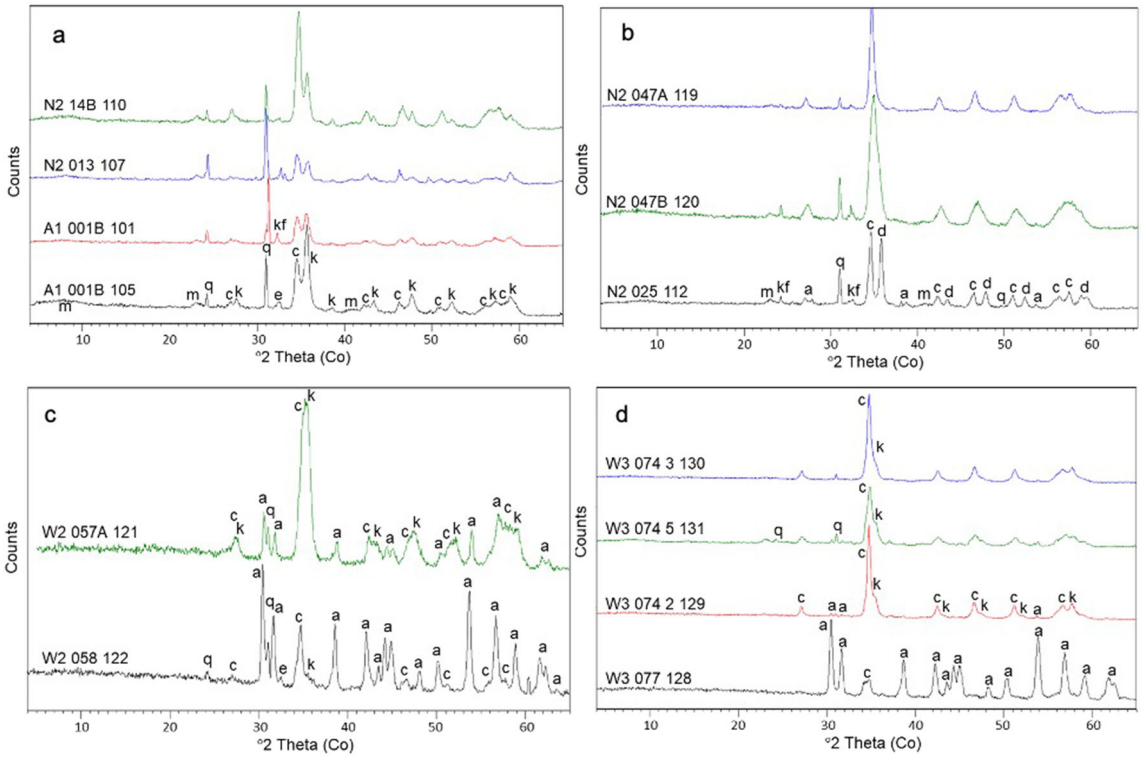

Fig. 7 X ray diffractograms of samples from the various sampling areas. Details of the mineralogical composition are given in the text; section mineralogical composition. Peak identification in the diffractograms is as follows: a—aragonite, c—calcite, d—dolomite, e—enstatite k—kutnohorite, Kf (K feldspar)—microcline, m—montmorolinite, q—quartz. (**a**) Acre A1: A1 001B 101, A1 001B 106 and Palmachim disturbance N2: N2 013 107 and N2 14B 110. (**b**) Palmachim disturbance N2: N2 025 112, N2 047B 120, N2 047A. (**c**) Palmachim disturbance W2: W2 058 122, N2 057A 121. (**d**) Palmachim disturbance W3: W3 077 128, W3 074 2 129, W3 074 5 131, W3 074 3 130

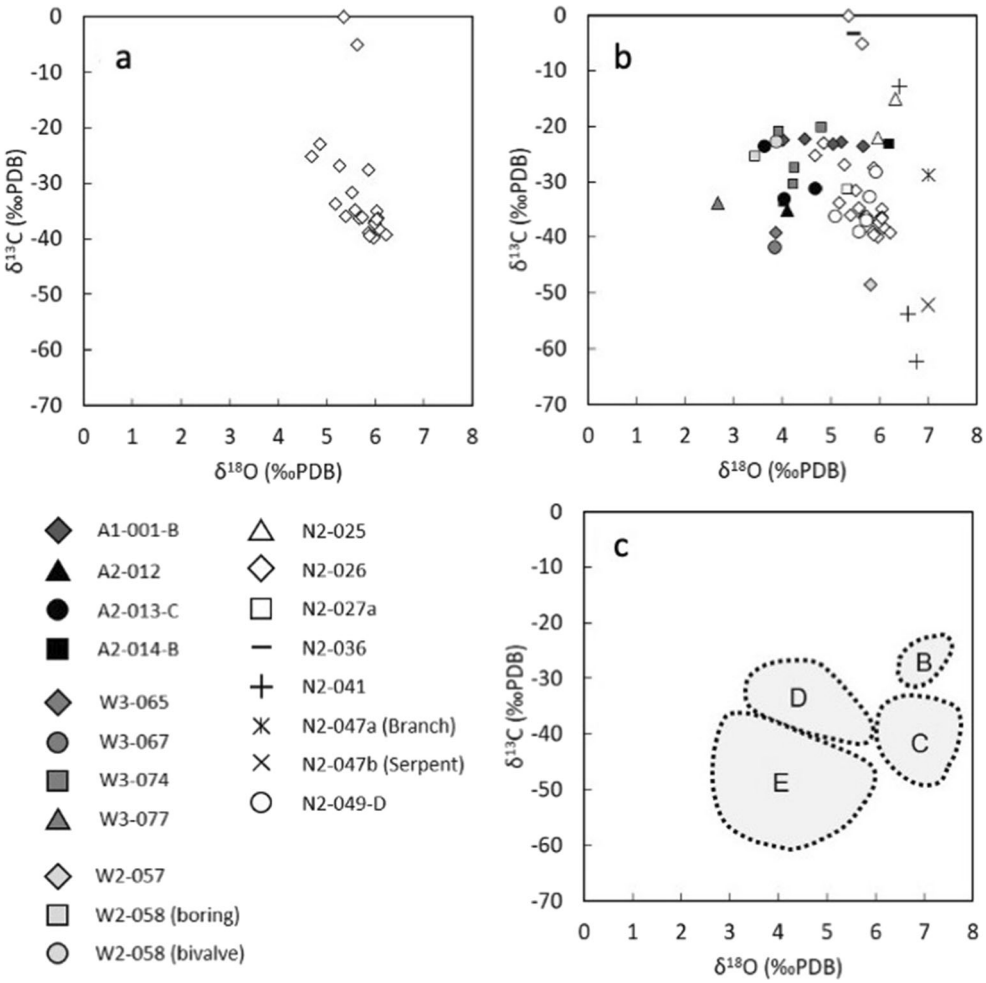

Fig. 8 $\delta^{13}C$ and $\delta^{18}O$ results. (**a**) Results for 026 chimney. (**b**) Results for all samples of the present study, marked according to areas. (**c**) Comparison: $\delta^{13}C$ and $\delta^{18}O$ values of samples from the Hydrate Ridge (Greinert et al. 2001)

dolomite to nearly pure magnesian calcite. The related $\delta^{13}C$ values range from −39.9 to 0.1‰PDB associated with $\delta^{18}O$ values from 6.2 to 4.7‰PDB. These isotopic indicators reflect the full spectrum from bacterial to thermogenic origin and indicate the dynamic nature of the contribution of organic carbon and the water feeding system, in the formation of this chimney. Similar $\delta^{13}C$ $\delta^{18}O$ trends and ranges were reported from dolomitic chimneys in the Gulf of Cadiz (Magalhaes et al. 2012). It is noteworthy that with decreasing proportion of dolomite, the peak of high Mg shifts to the left (decreasing 2θ values) (Fig. 5), indicating an increase in the Mg/Ca ratio.

The overall ranges of stable of C and O isotopes of the present study are as follows: $\delta^{13}C$ −62.0 to −0.1‰PDB which is narrower than that of the Hydrate Range, NE Pacific (Greinert et al. 2001) and of $\delta^{18}O$ values 2.7 to 7.0‰PDB which is also narrower than that reported from the Hydrate Range. This comparison provides general information on the geochemical data in view of the differences between the sites. It is noteworthy that group E of Greinert et al. (2001) (shown here in Fig. 8c), defined as "formation near the surface by methane oxidation by sulphate reduction", has a small representation in the present study. The composition of methane-related carbonate structures from deeper water environments (ca 2000m) in the Eastern Mediterranean, south of Crete (Aloisi et al. 2000), also have a wide range of $\delta^{13}C$ values (−48 to +5‰PDB), and a wide range of $\delta^{18}O$ values (1 to + 7‰PDB) in comparison with the results of this study ($\delta^{13}C$ values −62.3 to 0.1‰PDB, and $\delta^{18}O$ values 2.7 to 7.0‰PDB). These differences highlight the complexity of the systems and the variability in the factors that control them.

In the present study, no significant association was observed between sampling area and $\delta^{13}C$ values (Table 1). However, for the $\delta^{18}O$ values, a boundary at about 5‰PDB was identified. Nearly all samples from area N2 have $\delta^{18}O$ values >5‰PDB, including most of the aliquots of the large chimney sample 026, (except of sample 013C). On the other hand, the majority of samples from areas A1 and A2 offshore Acre, and areas W2 and W3 at the toe of the Palmachim disturbance have $\delta^{18}O$ values <5‰PDB (except of 014-B area A1 and two aliquots of sample 065 area W3).

This distinction in $\delta^{18}O$ values may represent a difference in the temperature of the fluids associated with the formation of the carbonate structures on the seabed; samples having $\delta^{18}O$

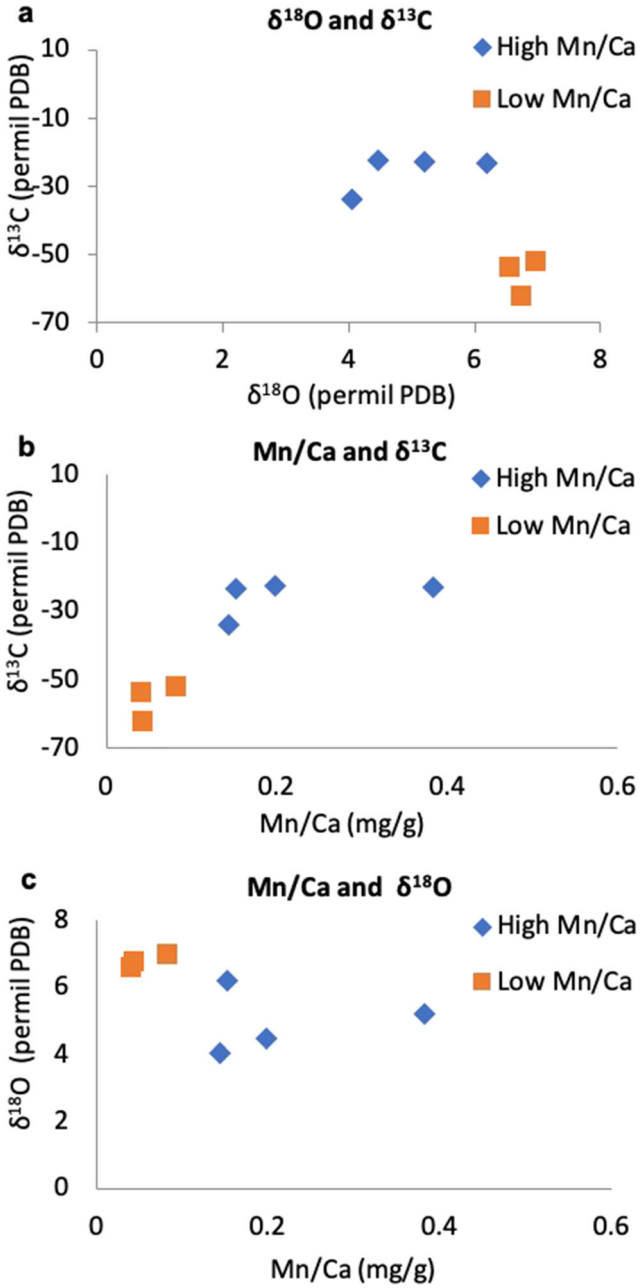

Fig. 9 Plots of $\delta^{13}C$, $\delta^{18}O$, and Mn/Ca in test samples in which kutnohorite was detected and samples in which it was not detected. (a) Plot $\delta^{13}C$ and $\delta^{18}O$ values of test samples in which kutnohorite was detected (diamonds) showing higher $\delta^{13}C$ and lower $\delta^{18}O$ values than in samples in which kutnohorite was not detected (squares). (b) Plot of Mn/Ca and $\delta^{13}C$ in test samples, showing an increase in $\delta^{13}C$ values with increase in Mn/Ca ratio. (c) Plot of Mn/Ca and $\delta^{18}O$ in test samples showing a slightly lower $\delta^{18}O$ values for samples having higher Mn/Ca ratios. These relationships indicate that the presence of kutnohorite (high Mn/Ca) is associated with higher $\delta^{13}C$, thermogenic methane, slightly lower $\delta^{18}O$ values higher temperature

<5‰PDB indicate that they formed at higher temperatures, reflecting the dominance of mineralising fluids of a deep source. This indication is observed in most samples from areas A1, A2, W2, and W3 and occurs in several samples of N2. In contrast, most samples from N2 have $\delta^{18}O$ values >5‰PDB associated with lower temperatures, fluids of shallow origin.

The record of the large chimney sample 026 from N2 crosses this boundary. This means that during the formation of this carbonate structure, the initial mineralising fluid was of high temperature but most of the chimney was deposited at low temperatures, in agreement with the increasing proportion of carbon of bacterial origin indicated by low $\delta^{13}C$ values.

The mineral kutnohorite Ca(Mn, Mg, Fe $^{2+}$) $(CO_3)_2$, which occurs in hydrothermal mineral deposits, was detected in the Hydrate Ridge (Greinert et al. 2001) and was detected in samples from areas A1 and A2 in the Acre area (Fig. 1). This area is close to a fault related to the Dead Sea transform fault system (Garfunkel 1998) a potential pathway for hydrothermal fluids, and in area W3, the toe of the Palmachim disturbance which is characterised by seafloor lineaments related to deep faults (Eruteya et al. 2018), where the presence of shallow gas was detected by geophysical methods. Kutnohorite was also detected in sample 013 from area N2 of the Palmachim disturbance which may be linked to the large boundary fault.

These features provide a new insight in that they indicate a link between the mineralogical characteristics of the carbonate structures. The occurrence, or otherwise, of kutnohorite (a mineral occurring in hydrothermal assemblages), the related chemical characteristic (high Mn/Ca ratio >0.1), low stable oxygen isotope values $\delta^{18}O$ <5‰, and the direct evidence of thermogenic methane (stable carbon isotope $\delta^{13}C$ >−35‰) allow for the identification of and distinction between carbonate assemblages formed in association with high-temperature fluids—thermogenic methane—and low-temperature fluids associated with bacterial methane.

The summary of the indicators of the carbonate structure for bacterial and thermogenic methane and associated fluid for the sites of the present study is: no kutnohorite—Mn/Ca rations <0.1, $\delta^{13}C$ < −35‰PDB are indicative of bacterial methane. In contrast, the presence of kutnohorite, Mn/Ca>0.1, $\delta^{13}C$ −35 to −20‰PDB indicate thermogenic methane. Furthermore, $\delta^{18}O$ carbonate >5‰PDB may indicate a shallow cold fluid associated with their formation, while $\delta^{18}O$ carbonate <5‰PDB is associated with a warm deep fluid.

This boundary of $\delta^{18}O$ values in methane-related carbonates differs between the Hydrate Ridge (Greinert et al. 2001) where it is at 6‰PDB and in the Eastern Mediterranean, the present study, where it is at 5‰PDB. Moreover, the signature of the isotopes that is retained in carbonate minerals, taken as indicative of carbon source and temperature, is governed by several factors. Therefore, the presence of an additional indicator, the mineral kutnohorite which is reflected in the higher Mn/Ca ratio of the samples, is a useful additional indicator for methane of thermogenic origin.

The hydrological and palaeoclimatic aspects of the present study are based on the distinction between carbonate deposits according to their oxygen isotope composition. The present

study of seabed carbonate structures indicates geographical and structural distinctions between areas A1 and A2 (fault zone offshore Acre) and W2 and W3 (toe of Palmachim disturbance) in contrast to area N (Fig. 2), which consists of an erosion surface of the shallow sediments of the Plamachim disturbance, but is crossed by its northern boundary fault. The first group has $\delta^{18}O$ carbonate <5‰PDB indicative of association with a warm deep fluid, while most of the samples from area N2 have $\delta^{18}O$ >5‰PDB which indicate that a cold shallow fluid associated with their formation, an indication supported by geophysical information showing the shallow sediments of the Palmachim deposit south of the northern boundary fault. Near the boundary fault samples have $\delta^{18}O$ <5‰PDB indicating warm deep fluids (Fig. 2).

This distinction may indicate that among the study areas, only this near-shore area was strongly influenced by emanations from the regional shallow Gas Hydrate Zone, the extent of which fluctuated between glacial and post-glacial periods (Praeg et al. 2011). The investigation of methane hydrates and their record in the form of carbonate deposits can provide information on palaeoclimate, as climate has major effects on the formation, alteration, and destruction of methane clathrates. A summary for the Mediterranean (Praeg et al. 2011) indicates that the Eastern Mediterranean is and was colder than the western Mediterranean, and that the gas hydrate stability zone (GHSZ) was larger in extent, thicker, and spreading to shallower depths during glacial periods. The glacial to interglacial transition corresponded to events of marked reduction in the stability of the GHSZ. Therefore, the extent and thickness of the GHSZ diminished, and it is likely that there was a downslope migration in the upper limit of its GHSZ across a depth range of ca. 700–1000 m. This in turn was associated with extensive submarine landslides during that period, resulting in headwalls in mid or upper parts of the slope (Praeg et al. 2011).

Conclusions

Four indicators can help distinguish between seabed carbonate structures generated from thermogenic methane associated with fluids of high temperatures, from those derived from bacterial methane associated with fluids of low temperatures. These were identified in the Eastern Mediterranean offshore Israel by the following characteristics: (1) mineralogical—the presence or otherwise of the mineral kutnohorite, (2) chemical—Mn/Ca (wt./wt.) values higher or lower than 0.1, (3) $\delta^{13}C$ carbonate values, higher or lower than about −35‰PDB, (4) $\delta^{18}O$ carbonate values, lower or higher than 5‰PDB respectively. These indications obtained from surficial carbonate structures may be useful in the early stages of exploration.

Indications of thermogenic methane were detected in the Acre area, located near a fault system belonging to the Dead Sea Rift system, and also at the toe (deeper part) of a large slump (Palmachim disturbance), indicating some structural control. The results for area N2 of the Palmachim disturbance include indications of both microbial and thermogenic origin. The first occurs in the southern part of the area where the likely methane source are the shallow sediments exposed by the structural deformation and subsequent erosion. In contrast, the northern sampling sites are close to the northern boundary fault of the Palmachim disturbance which is the likely conduit of the deep thermogenic methane.

The effect of climate-palaeoclimate can be discerned in most of the samples from area N2 of the Palmachim disturbance as they have $\delta^{18}O$ >5‰PDB, indicative of a cold shallow fluid associated with their formation. These values may be linked to emanations from the regional Gas Hydrate Zone, which was widespread in this area of the Eastern Mediterranean during the ice ages. These findings may be of wide interest, as shallow methane of gas hydrate origin may constitute a resource, in addition to the large thermogenic gas resources of the Eastern Mediterranean.

Acknowledgements We thank Dr Emma Humphreys-Williams for the chemical analyses. We thank Dr Andrew Green, the Editor-in-chief of Geo-Marine Letters, for his dedication and help.

References

Aharon P, Fu B (2000) Microbial sulphate reduction rates and sulphur and oxygen isotope fractionations at oil and gas seeps in deepwater Gulf of Mexico Geochim. et Cosmochim. Acta 64:233–224

Almagor G, Gill D, Perath I (2000) Marine sand resources offshore Israel. Mar Georesour Geotechnol 18(1):1–42

Aloisi G, Pierre C, Rouchy JM, Foucher JP, Woodside J, MEDINAUT Scientific Party (2000) Methane-related authigenic carbonates of eastern Mediterranean Sea mud volcanoes and their possible relation to gas hydrate destabilisation. Earth Planetary Science letters 184: 321–338

Astrakhov AS, Tiedman RA, Mudramaa IO, Bogdanova Y, Mozhorovky AV, Sereda A (2008) Marine geology of manganese carbonates in the Upper Quaternary sediment of the Deryugin Basin (Sea of Okhotsk). Oceanology 46:716–729. https://doi.org/10.1134/SOO1437006050122

Dickens GR (2003) Rethinking the global carbon cycle with large, dynamic and microbially mediated gas hydrate capacitor. Earth Planetary Science letters 213:169–183

Eruteya OE, Reshef M, Ben Avraham Z, Waldman V (2018) Gas escape along Palmachim disturbance in the Levant Basin offshore Israel. Marine Petroleum Geology 92:868–879

Ezra O (2016) Topology and formation settings of deep water carbonates at the boundary of the Palmachim disturbance, off-shore Israel. Leon H. Charney School of Marine Sciences University of Haifa 77P.

Feinstein S, Aizenshtat Z, Miloslavski I, Gerling P, Slager J, McQuilken J (2002) Genetic characterization of gas shows in the east Mediterranean offshore of southwestern Israel. Org Geochem 33(12):1401–1413

Garcia-Alix A, Jimenez-Moreno G, Jimenez-Espejo FJ, Garcia-Garcia F, Delgado-Huertas A (2014) An environmental snapshot of the Bolling interstadial in Southern Iberia. Quaternary Research 81: 284–294

Garfunkel Z (1998) Constraints on the origin and history of the Eastern Mediterranean basin. Tectonophysics 298:5–35

Garfunkel Z, Arad A, Almagor G (1979) The Palmachim disturbance and its regional setting. Geological Survey of Israel Bulletin No 72. Geological Survey of Israel 56P

Greinert J, Bohrmann G, Suess E (2001) Gas Hydrate-Associated carbonates and methane-venting at Hydrate Ridge classification distribution and origin of authigenic lithologies. In: Pauli CK, Dillon WK (eds) Natural Gas Hydrates Occurrence, Distribution and Detection. Geophysical Monograph 124 American Geophysical Union, pp 99–113

Hashikubo A, Kosaka T, Kida M, Krylov A, Sakagami H, Minami H, Takahashi N, Shoji H (2007) Isotopic fractionation of methane and ethane hydrates between gas and hydrate phases. Geophysical Research Letters 34:L21502. https://doi.org/10.1029/2007GL030557

Jørgensen BB (1977) The sulphur cycle of a coastal marine sediment (Limfjorden, Denmark). Limnology and oceanography 22:814–832

Joseph C, Campbell KA, Torres ME, Martin RA, Pohlman JW, Riedel M, Rose K (2013) Methane-derived authigenic carbonates from modern and palaeoseeps on the Cascadia margin: Mechanisms of formation and diagenetic signals. Palaeogeography, Palaeoclimatology, Palaeoecology 390:52–67

Judd G, Hovland M (1992) The evidence of shallow gas in marine sediments. Continental shelf Research 12:1081–1095

Katz O, Einav R, Aharonov E (2015) Submarine landslides and fault scarps in the eastern Mediterranean Israeli continental slope. Marine Geology 369:100–115

Magalhaes VH, Pinheiro LM, Ivanov MK, et al. (10 more) (2012) Formation processes of methane-derived authigenic carbonates from the Gulf of Cadiz. Sedimentary Geology 243-244 155-168

Mucci A (1991) The solubility and free energy of formation of natural kutnahorite. American mineralogist 29:113–121

Praeg D, Geletti R, Warfell N, Unnitham V, Mascle J, Migeon S, Camerlenghi A (2011) Proceedings of the 7th Hydrate International Conference on Gas Hydrates.

Rubin-Blum M, Antler G, Turchyn AV, Tsadok R, Goodman-Tchernov BN, Shemesh E, Austin JA, Coleman DF, Makovsky Y, Sivan O, Tchernov D (2014) Hydrocarbon-related microbial processes in the deep sediments of the Eastern Mediterranean Levantine Basin. FEMS Microbiol Ecol 87:780–796

Schoell M (1984) Recent advances in petroleum isotope geochemistry. Organic Geochemistry 6:645–663

Shaffer B (2011) New natural gas producer in the Mediterranean. Energy Policy 39:5379–5387

Tissot BP, Welte DH (1984) Petroleum Formation and Occurrence 2nd Ed. Springer 699 pp.

Vandré C, Cramer B, Gerling P, Winsemann J (2007) Natural gas formation in the western Nile delta (Eastern Mediterranean): Thermogenic versus microbial. Organic Geochemistry 38:523–539

Whiticar MJ (1999) Carbon and hydrogen isotope systematics of bacterial formation and oxidation of methane. Chemical Geology 161:291–314